We are IntechOpen,
the world's leading publisher of Open Access books
Built by scientists, for scientists

6,900
Open access books available

186,000
International authors and editors

200M
Downloads

Our authors are among the

154
Countries delivered to

TOP 1%
most cited scientists

12.2%
Contributors from top 500 universities

CLARIVATE ANALYTICS
BOOK CITATION INDEX
INDEXED

WEB OF SCIENCE™

Selection of our books indexed in the Book Citation Index
in Web of Science™ Core Collection (BKCI)

Interested in publishing with us?
Contact book.department@intechopen.com

Numbers displayed above are based on latest data collected.
For more information visit www.intechopen.com

Chapter

Harnessing the Automotive Waste Heat with Thermoelectric Modules Using Maximum Power Point Tracking Method

Dario Gandini, Marcello Chiaberge and Andrea Nepote

Abstract

The present work shows a comprehensive methodology and design steps to recover energy from the automotive waste heat. A thermoelectric generator must be connected to a power converter in order to extract the maximum power from the generator and, also, satisfy different constrains to charge a battery. Starting from the electrical model of thermoelectric cells, it is evaluated their combination to realize a thermoelectric generator (TEG) comply with the automotive regulation, then considering input/output electric characteristics, it is evaluated the best converter topology to satisfy all constrains. Design steps and power dissipation estimation are deeply explained. TEG and power converter models are simulated in a model-based environment to allow the design of the control algorithms. The control system consists of nested control loops. Two maximum power point tracking (MPPT) algorithms are evaluated. The MPPT output is used as reference for a current control loop. The maximum power characteristic of a TEG has a quadratic behavior and working without the tracking of the maximum power point could drastically decrease the generated power from the TEG and the system efficiency. There are presented simulation results of the control algorithms and experimental data are shown in order to validate the design steps.

Keywords: automotive, thermoelectric generator, waste heat, storage, DC-DC converter, MPPT

1. Introduction

Nowadays the reuse of wasted energy is an important task for many fields, particularly for the automotive one. This aims at more efficient systems, reducing pollution and making the product more compatible with the environment, regulations, and consumers. Internal combustion engine vehicles do not totally convert the chemical energy into mechanical, the greater part of a typical fuel path is wasted in the coolant system and in the exhaust, and according to Chuang and Chau [1], only 25% of the energy flows into specific vehicle operations (**Figure 1**). The strategy is to convert the heat wasted energy into electricity by means of a thermo-electric generator (TEG), which is based on the Seebeck effect. Heat flows through

the TEG that, thanks to the difference of temperature (ΔT) between the hot and cold sides, generates electrical power that flows into the connected load. **Figure 2** shows the quantities that interact with the TEG: heat, temperature, thermal resistance, interface material, and electrical quantities.

The increase of delta temperature also increases the available power, but for each delta temperature, there is only one maximum power that can be generated connecting a precise load. A simple approach is to connect a DC-DC converter after the TEG. The DC-DC converter can set the current flow; thus, from the TEG point of view, it acts as a variable load. Specific control algorithms can be implemented
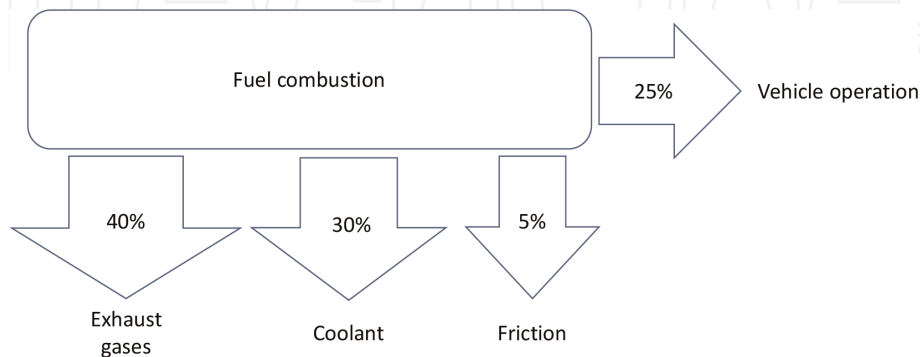

Figure 1.
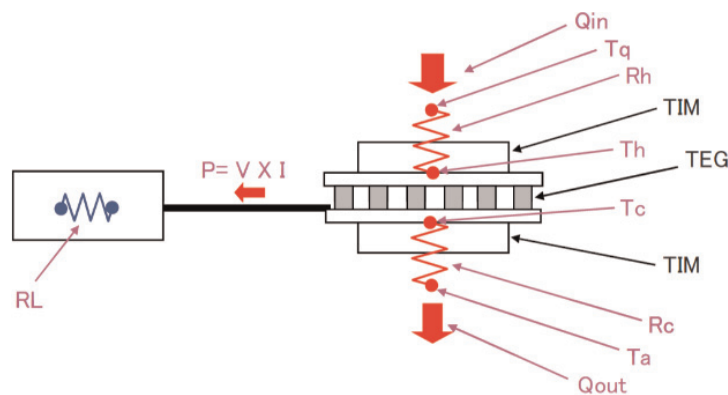*Quantity of energy used for the vehicle operation.*

Figure 2.
TEG quantities. Q_{in} is the heat quantity to flow into TEG, Q_{out} is the heat quantity to flow out of TEG, T_q is the temperature of heat source, T_a is the temperature of ambient (cold source), T_h is the temperature of TEG hot-side surface, T_c is the temperature of TEG cold-side surface, TIM is the thermal interface material, R_h is the heat resistance of TIM between TEG and heat source, R_c is the heat resistance of TIM between TEG and ambient, P is the electrical power, V is the voltage, I is the current, and RL is the load resistance.
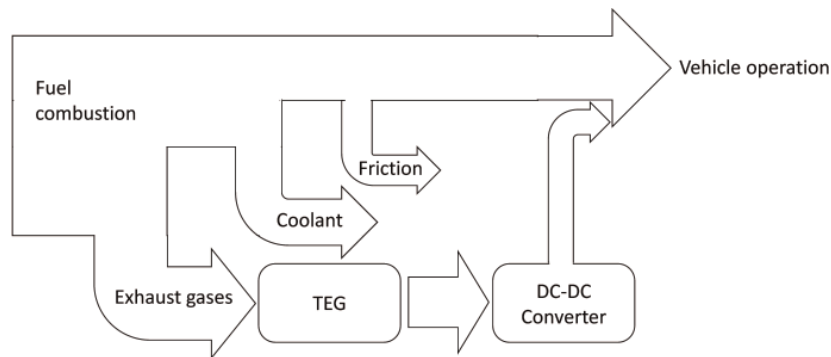

Figure 3.
Diagram of the wasted heat energy recovery system.

into the converter in order for each delta temperature to be the correct load. The converter output can be connected to the vehicle battery, so the generated power can be directly used for vehicle operations or stored for future needs. The described system allows to recover part of the wasted energy increasing the total efficiency of the vehicle. **Figure 3** shows a conceptual diagram of the system from fuel combustion to wasted heat and the recovery system, TEG plus DC-DC, that generates power useful for vehicle operations.

2. Design methodology of an energy recovery system

This chapter describes a comprehensive methodology for the design of an energy recovery system. Starting from physical characteristics of the generator, its electrical model is obtained. Since the generator under examination is a thermoelectric generator, all derived parameters will be expressed as a function of the delta temperature, the temperature difference between the hot and cold sides of the generator. Firstly, it is characterized and modeled a single thermoelectric cell, then it is designed the cells combination to make the TEG generator: the resulting equivalent electrical model of the generator is similar to a single cell with grater voltage and current parameters. The parameters obtained by the generator model are used as constraint for the DC-DC converter topology definition, and the design steps are described, highlighting the necessary trade-offs. After these stages it is possible to face the control algorithms. In order to design a control algorithm, there are two necessary information: what the target is and what the weapons are to reach the target. Finally, the single sections are put together in a single simulation environment where it is possible to test the global system changing temperature and load conditions.

2.1 TEG and its electrical model

Figure 4 shows the open-circuit voltage and the maximum power characteristics of the hypotetical thermoelectric cell. They are represented as a function of the delta temperature across the cell. The maximum allowed delta temperature is 180° C. The open-circuit voltage (V_{OC}) grows linearly with the delta temperature (Eq. (1)), while the available maximum power (P_{MAX}) has a parabolic behavior (Eq. (2)). The maximum open-circuit output voltage is almost 8 V, and the
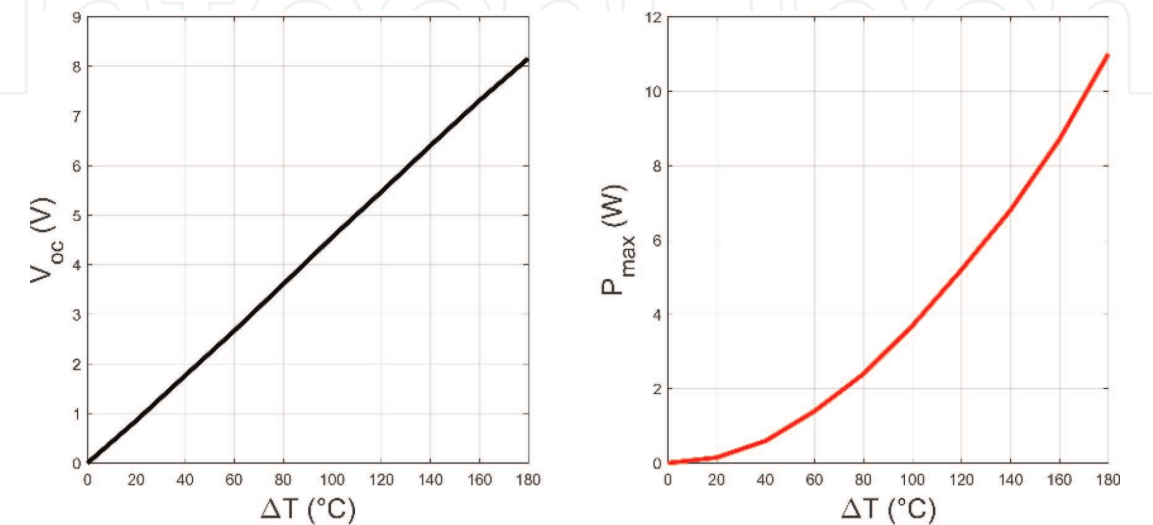

Figure 4.
TEG cell characteristics as a function of delta temperature; on the left the open-circuit voltage and on the right the available maximum power.

maximum power is a little more than 10 W. The coefficients m_v and m_p are specifics of the selected TEG cell:

$$V_{OC} = m_v \cdot \Delta T \tag{1}$$

$$P_{MAX} = m_p \cdot \Delta T^2 \tag{2}$$

Figure 5 shows the voltage-current and the power-voltage characteristics at a single delta temperature. When the TEG output is closed in short circuit, the voltage is zero, and the output current reach is local maximum (I_{sc}). It is important, with the purpose of generating the available maximum power, to know, for each delta temperature, the correct voltage-current couple. In Eq. (3) the relation between the voltage to generate the maximum power (V_{mpp}) and the open-circuit voltage is pointed out, namely, the delta temperature. In Eq. (4) the current to generate the maximum power (I_{mpp}) is derived as a function of the already calculated parameters:

$$V_{mpp} = \frac{V_{OC}}{2} = \frac{m_v}{2} \cdot \Delta T \tag{3}$$

$$I_{mpp} = \frac{P_{MAX}}{V_{mpp}} = \frac{2 \cdot m_p}{m_v} \cdot \Delta T \tag{4}$$

From the voltage-current characteristic, it is also possible to extract the value of the TEG equivalent series resistance (Eq. (5)). **Figure 6** shows the voltage-current characteristic at different delta temperature: different slopes mean different equivalent resistance:

$$R_{eq} = \left| \frac{I_{sc}}{-V_{oc}} \right| \tag{5}$$

Figure 7 shows the equivalent series resistance calculated at different delta temperature. Eq. (6) shows the equivalent series resistance as a function of delta temperature. The equivalent electric model of a TEG cell is a variable voltage
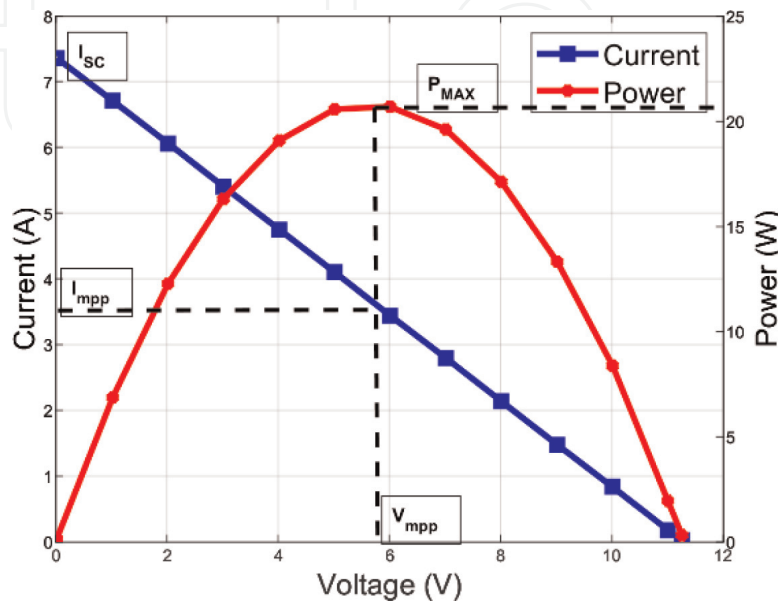

Figure 5.
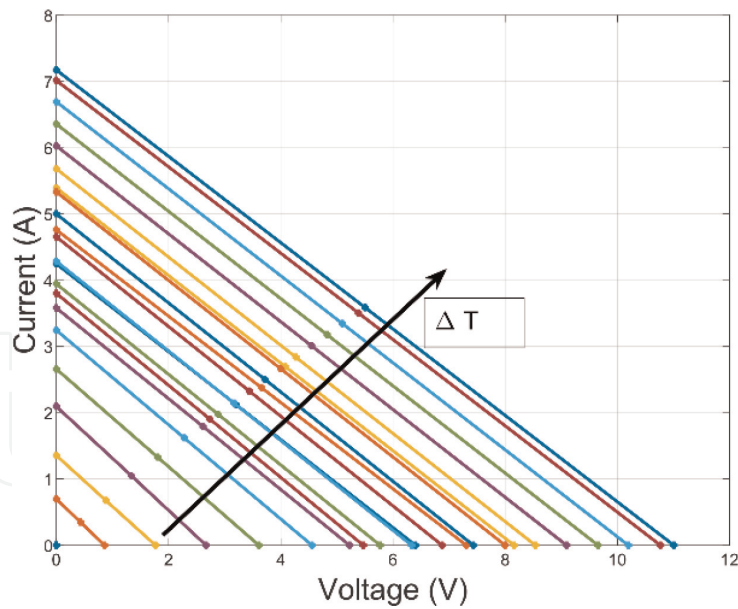*Current-voltage and power-voltage characteristics.*

Figure 6.
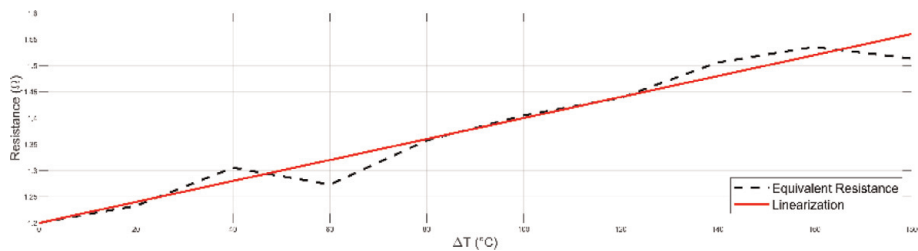*Equivalent resistance as a function of temperature difference.*

Figure 7.
TEG equivalent resistance as a function of delta temperature.

generator with a variable series resistance, both proportional of the delta temperature:

$$R_{eq} = m_r \cdot \Delta T + q_r \tag{6}$$

More TEG cells can be combined in order to increase the total generated power. Combination can be done by putting the cells in series, increasing output voltage, or, in parallel, increasing the output current. Due to regulatory constraint, it is better to keep the maximum voltage under 60 V. Furthermore, the TEG pack design is strictly related to available space, point of contact of the exhaust pipe, and heat cooling passing through the TEG (it will cause different available powers between near cells) [2, 3]. The TEG pack for this application is constituted by six cells in series and four in parallel. **Figure 8** shows the equivalent electric model of the TEG pack constituted by 24 cells. Under the hypothesis of a good pack design, Eqs. (7)–(12) give a general relation between electrical parameters and the number of cells in series (C_s) and in parallel (C_p):

$$V'_{oc} = V_{OC} \cdot C_s \tag{7}$$

$$R'_{eq} = R_{eq} \cdot \frac{C_s}{C_p} \tag{8}$$

$$P'_{max} = \left(V'_{oc}\right)^2 / R'_{eq} \tag{9}$$

$$I'_{sc} = I_{sc} \cdot C_p \tag{10}$$

$$V'_{mpp} = V_{mpp} \cdot C_s \tag{11}$$

$$I'_{mpp} = I_{mpp} \cdot C_p \tag{12}$$

2.2 DC-DC topology evaluation

Usually the aim of a DC-DC converter is to regulate an unregulated input voltage for a specific load; in this application the final goal is to take the maximum power from the generator at the larger possible temperature excursion, namely, manage a wide input voltage and set the current flows. A battery is connected to the output, so the output voltage must be slightly higher than the battery voltage, in order to allow the recharge. The battery voltage is set at 12 V. The input voltage is supposed to be in the range from 0 to 60 V.

Every DC-DC topology has its own relation between input and output voltages. In this test case, commonly used topologies, like buck or boost converter, are excluded. A buck converter (**Figure 9**) works only with input voltage higher than output; it means only with high delta temperature. A boost converter (**Figure 10**) works only with input voltage lower than output; it means only with low delta temperature. In order to manage input voltage lower and higher than the output, it
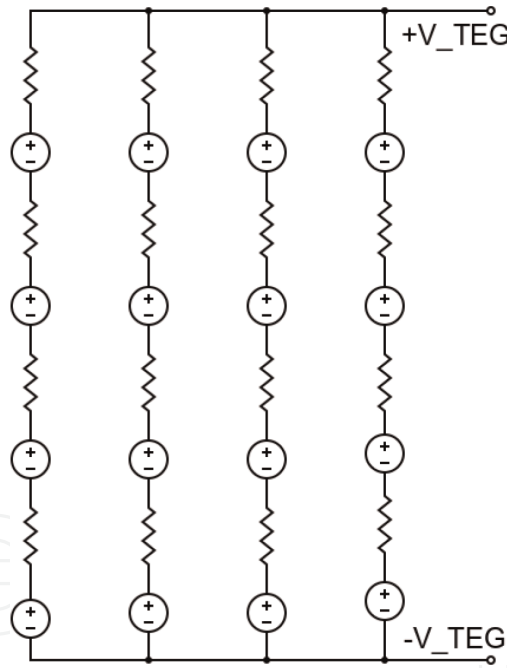
Figure 8.
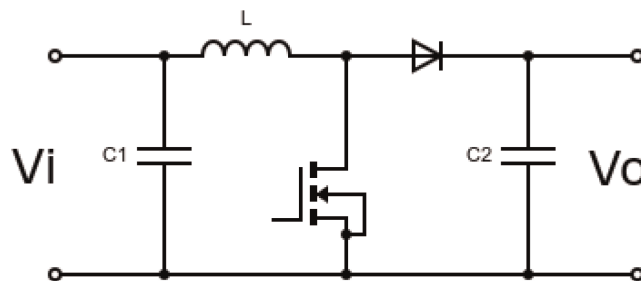*TEG cell configuration electrical equivalent.*

Figure 9.
Boost converter topology.

is possible to combine these two topologies. From the combination of a buck and boost converters, there are two topologies:

- Boost and buck cascaded

- Non-inverting buck-boost (NIBB)

In the boost and buck cascaded topology, there are two stages: the first one is a boost stage, and the second is a buck stage. Both stages have their own inductor (**Figure 11**). If the input voltage is lower than the output voltage, only the first stage works, while the high-side switch belonging to the second stage is always closed; on the other hand, if the input voltage is higher than the output voltage, only the second stage works, while the low-side switch belonging to the first stage is always open. As a third working option, if the input voltage is near the output voltage, both stages could work: the boost stage slightly increases the input voltage, and the buck stage regulates and complies with the desired output voltage.

In the non-inverting buck-boost topology, the two stages are compressed, and there is only one inductor that is shared by them (**Figure 12**). The first leg is
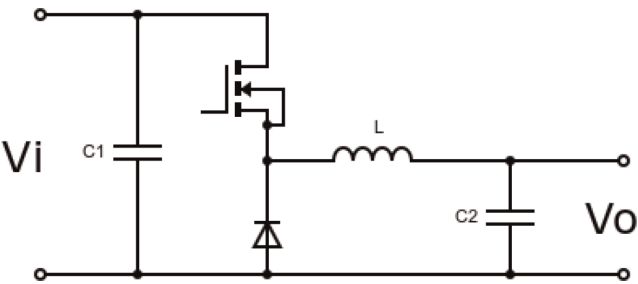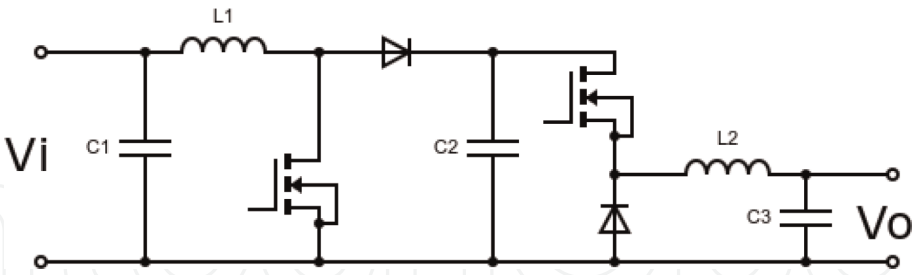

Figure 10.
Buck converter topology.

Figure 11.
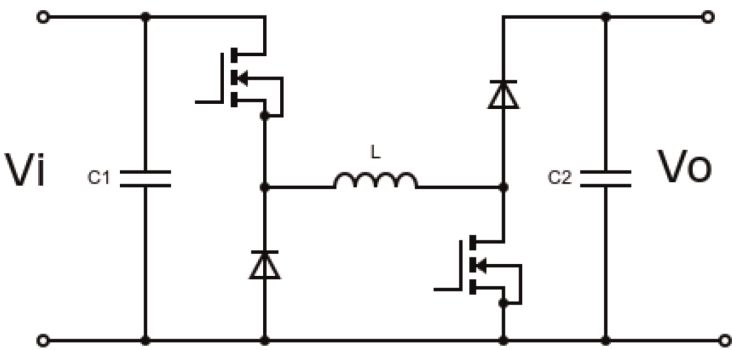*Boost and buck cascaded topology.*

Figure 12.
Non-inverting buck-boost (NIBB) topology.

dedicated for buck operation, while the second leg for the boost operation. As in the previous topology, it is possible to manage input voltage that is lower or higher than the output voltage. The three working regions are:

- Buck (Vi > Vo)

- Boost (Vi < Vo)

- Buck-boost (Vi ≈ Vo)

Practically the inductor is shared only in the buck-boost working region; on the other only one leg is active, and the other has a fixed state. In order to reduce weight, number of components, and loss sources, the NIBB topology is the perfect candidate for this application. In the next section, design steps and loss estimation of the NIBB topology are presented.

2.3 NIBB design

In the non-inverting buck-boost topology, a buck and a boost are fused together and share a single inductor. A technique for improving the converter's efficiency is the synchronous rectification. The two versions of the NIBB converter are also called two-switch and four-switch non-inverting buck-boost. The two-switch NIBB (2SW-NIBB) has diodes, while in the four-switch NIBB (4SW-NIBB), the diodes are replaced by power MOSFETs (**Figure 13**). This topology will be used for the DC-DC converter, and in the following, the design steps are reported.
Below the starting specifications for the design are reported:

- Input voltage $0 < Vi < 60$ V.

- $V_o \approx 12$ V.

- Maximum output power 300 W.

- Output power is proportional to input voltage.

The steady-state relation between input and output voltages of a 4SW-NIBB is outlined in Eq. (13). D_A and D_B are the commands of the switches, namely, duty cycles; their range is from 0 to 1. D_A is the duty cycle of the buck leg high-side switch; the command of the low-side switch is $1 - D_A$ ($\overline{D_A}$). D_B is the duty cycle of
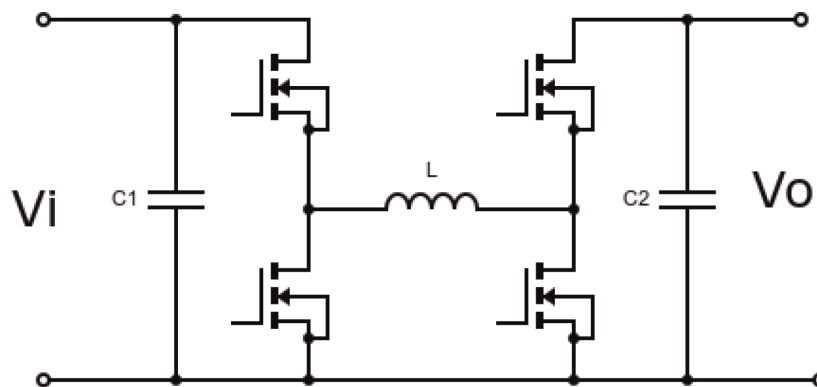

Figure 13.
NIBB with synchronous rectification (4SW-NIBB) circuit.

the boost leg (low-side switch); the command of the high-side switch is $1 - D_B$ ($\overline{D_B}$):

$$V_o = \frac{V_i \cdot D_A}{1 - D_B} \tag{13}$$

It is known from Section 2.1 that to extract the maximum power from the TEG, its output voltage must be half of the open-circuit voltage; in the following V_{mpp} is considered as the effective input voltage of the DC-DC converter. **Figure 14** shows the relation between V_{mpp} and delta temperature, highlighting the working regions. The general relation between input and output voltages could be simplified considering in which region the converter is working (Eq. (14)):

$$\begin{cases} V_o = \dfrac{V_i}{1 - D_B}, D_A = 1 \ (Boost \ region) \\[2mm] V_o = \dfrac{V_i \cdot D_A}{1 - D_B} \ (Buck - Boost \ region) \\[2mm] V_o = V_i \cdot D_A, D_B = 0 \ (Buck \ region) \end{cases} \tag{14}$$

In order to define switching frequency and inductor value, the two operation modes of a DC-DC converter are introduced: continuous current mode (CCM) and discontinuous current mode (DCM). The DCM operation is characterized by a current of the inductor that is zero during the switching period, while in the CCM, the inductor current never reduces to zero (**Figure 15**). The DCM operation is particularly a disadvantage for the buck region. In order to avoid the DCM operation for the buck working region, Eq. (15) must be verified. The value of L_{crit} is calculated in Eq. (16), where ΔI_L is the current ripple on the inductor and can be considered a percentage of the output current, typically 20–30% of the output current:

$$L > L_{crit} \tag{15}$$

$$L_{crit} = D_A \cdot \frac{V_i - V_o}{\Delta I_L \cdot f_{SW}} \tag{16}$$
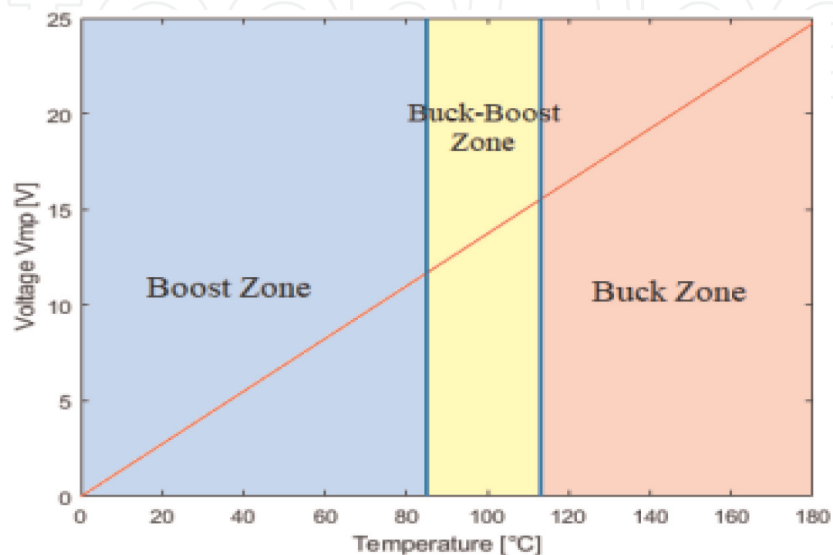

Figure 14.
Converter input voltage as a function of the temperature difference, highlighting working regions.

Figure 16 shows the relation between L_{crit} and the temperature difference considering different switching frequency. The use of high switching frequency allows the use of smaller inductor but means higher switching losses. The switching frequency and the inductor value are a trade-off between reduced component dimension and losses. The last important parameter for the inductor selection is the saturation current that is calculated in Eq. (17), where μ is the converter efficiency that as a safety factor can be set to 80%:

$$I_{L,sat} = \frac{V_o \cdot I_o}{\mu \cdot V_{in}} + \frac{\Delta I_L}{2} \qquad (17)$$

The capacitor selection is based on maximum RMS current that is flown into it and the voltage ripple. The output capacitor selection is based on the maximum RMS current in the capacitor during the boost working region and the output voltage ripple specification. Maximum RMS current in the output capacitor is calculated in Eq. (18). Input voltage is the maximum input voltage for the boost working region. The output voltage ripple has two contributions: the first one due to capacitor equivalent series resistance (ESR) and the other related to capacitance (Eq. (19)):

$$I_{C_O,RMS} = I_o \sqrt{\frac{V_o}{V_{IN}}} \qquad (18)$$

$$\Delta V_{C_O} = \frac{I_o V_o}{V_{in}} \cdot ESR + \frac{I_o}{C_o \cdot f_{SW}} \left(\frac{V_o - V_{in}}{V_o} \right) \qquad (19)$$
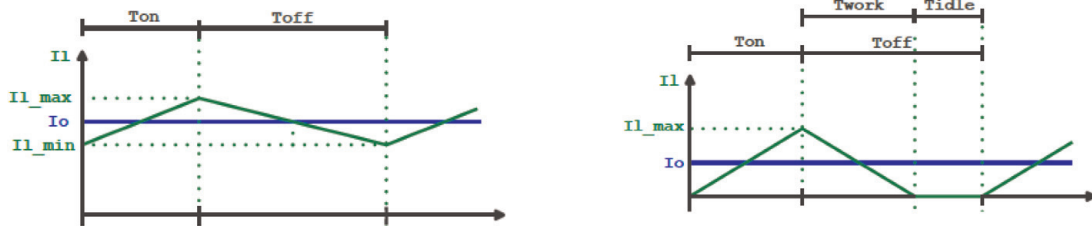

Figure 15.
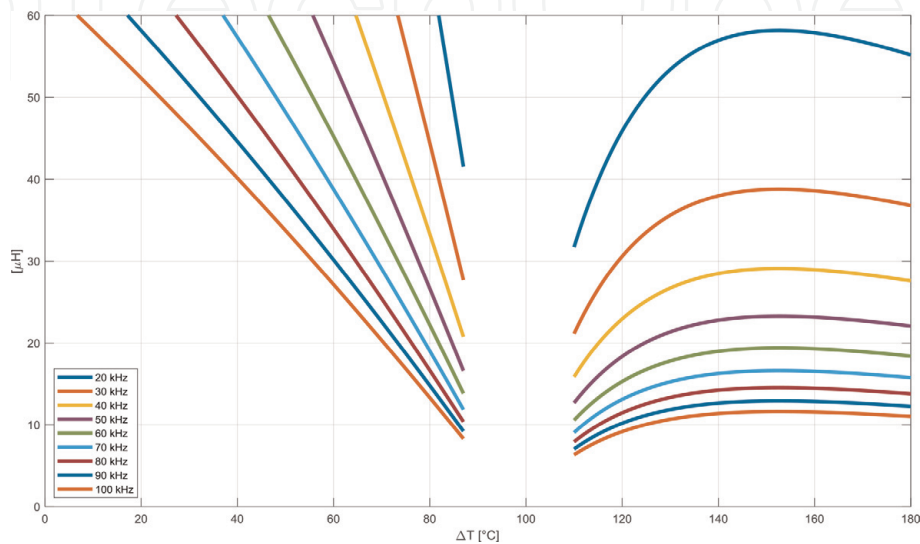*Inductor current waveform: (left) CCM and (right) DCM.*

Figure 16.
Minimum CCM inductance as a function of temperature difference.

Input capacitor selection closely follows the method used for the output capacitor. The maximum RMS current flowing in CIN occurs in buck mode that is calculated in Eq. (20). As for the output capacitance, the input voltage ripple has two contributions: the first one related to input capacitor ESR and the second due to capacitance (Eq. (21)):

$$\mathrm{I}_{\mathrm{C_{in}},\,RMS} = \sqrt{\frac{V_o}{V_{IN}}\left[I_o^2\left(1-\frac{V_o}{V_{in}}\right)+\frac{1}{12}\Delta I_L^2\right]} \tag{20}$$

$$\Delta V_{C_{in}} = I_o \cdot ESR + \frac{I_o \cdot V_o}{V_{in} \cdot C_{in} \cdot f_{SW}}\left(1-\frac{V_o}{V_{in}}\right) \tag{21}$$

2.3.1 Loss estimation

At first approximation inductor and capacitors are due to the component's equivalent series resistance (ESR). In Eqs. (22) and (23), the input capacitor losses and output capacitor losses are calculated, respectively; inductor losses are calculated in Eq. (24):

$$\mathrm{P}_{\mathrm{C_{in}}}(\Delta T) = ESR_{C_{in}} \cdot \mathrm{I}_{\mathrm{C_{in},\,RMS}}^2(\Delta T) \tag{22}$$

$$\mathrm{P}_{\mathrm{C_o}}(\Delta T) = ESR_{C_o} \cdot \mathrm{I}_{\mathrm{C_o,\,RMS}}^2(\Delta T) \tag{23}$$

$$\mathrm{P}_L(\Delta T) = ESR_L \cdot \mathrm{I}_o^2(\Delta T) \tag{24}$$

The MOSFET losses have two components: conduction and switching losses. Conduction losses are calculated in Eq. (25). R_{dson} is the equivalent resistance of the MOSFET when it is closed. For the switching losses, it is necessary to separate the two legs: Eq. (26) for the buck leg and Eq. (27) for the boost leg. t_R is the rise time and t_F is the fall time, parameters of the selected switch. While output current is a constraint of the application, the switching frequency is a degree of freedom that can be used in order to reduce switching losses (**Figures 17** and **18**):

$$P_{cond}(\Delta T) = 2 \cdot R_{dson} \cdot \mathrm{I}_o^2(\Delta T) \tag{25}$$
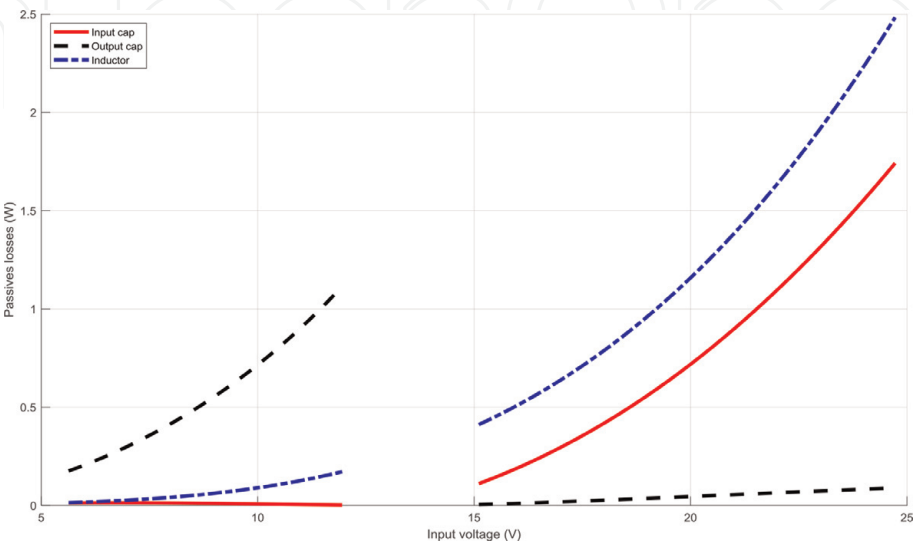

Figure 17.
*Loss estimation of the passive components. Continuous line input capacitor; dashed line is the output capacitor; dash-dotted line is the inductor. Parameters of **Table 1**.*
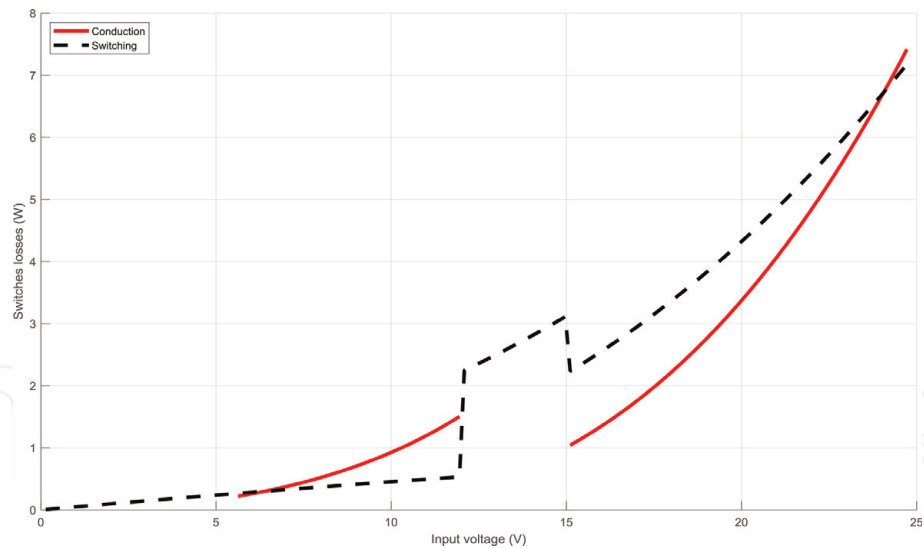
Figure 18.
Loss estimation of the switches. Continuous line is the conduction losses; dashed lines are the switching losses.
*Parameters of **Table 1**.*

Parameter/component	Value
f_{sw}	30 kHz
L	30 µH
L ESR	20 mΩ
C_{in}	660 µF
ESR C_{in}	20 mΩ
C_{out}	330 µF
ESR C_{out}	40 mΩ
$R_{ds,ON}$	5 mΩ
t_R	350 ns
t_F	200 ns

Table 1.
Summary of the converter design.

$$P_{sw}(\Delta T) = f_{sw} \cdot (t_R + t_F) \cdot V_{mpp}(\Delta T) \cdot I_o(\Delta T) \qquad (26)$$

$$P_{sw}(\Delta T) = f_{sw} \cdot (t_R + t_F) \cdot V_o \cdot I_o(\Delta T) \qquad (27)$$

The final design is a trade-off between inductor and capacitor values, namely, dimension and weight, and the losses. **Table 1** shows the summary of the design. Device's parameters are comparable with real components available on the market. These parameters are used for the control algorithms and simulation sections.

2.4 Control algorithms

The control system consists of nested control loops. In order to extract the maximum power from the TEG, two different maximum power point tracking (MPPT) algorithms are evaluated. The MPPT output is used as reference for voltage and current control loops. Analog variables are input and output voltage and current of the converter; commands are the duty cycles of the legs. Input voltage and

current are used for the maximum power point tracking; output voltage and current are used for the other control loops.

2.4.1 Maximum power point tracking

There are many MPPT algorithms that are suitable for use with a TEG, most of which have been adapted from those used by photovoltaic systems [4]. The most common are perturb and observe (P&O) and incremental conductance (IC) algorithms [5–8]. P&O algorithm is an iterative algorithm, its working principle is to introduce a perturbation in the operating voltage and current, and then the operating power is observed and compared with the power of the previous step. If the power difference is positive (negative), subsequently the MPP will be reached if the perturbation is stepped in the same (opposite) direction. The flowchart for P&O is shown in **Figure 19**. A P&O algorithm cannot determine if the MPP is reached: when it does reach it, it will pass the operating voltage beyond which will result in a decrease of power; in response the algorithm will reverse the tracking direction. Therefore, in employing a P&O algorithm, the operating point oscillates around the MPP. In order to reduce the oscillation, it is possible to make the perturbation size smaller. However, reducing perturbation size means reducing the algorithm dynamics and increasing the time to reach the MPP. A trade-off between steady-state performance and dynamic response is the use of variable perturbation size [9, 10].

In order to improve the steady-state error, the incremental conductance (IC) algorithm was implemented. It tracks by stepping the voltage like the P&O, and it operates by incrementally comparing the ratio of the derivative of conductance (dI/dV) with the instantaneous conductance (I/V). The advantage of using IC method with respect to the P&O is that it can determine the MPP; in fact, at MPP, the derivative of power with respect to voltage (dP/dV) is 0. The relation between conductance and power-voltage ratio is expressed in Eq. (28). The basic rules for IC are written in Eq. (29). The IC algorithm flowchart is reported in **Figure 20**:
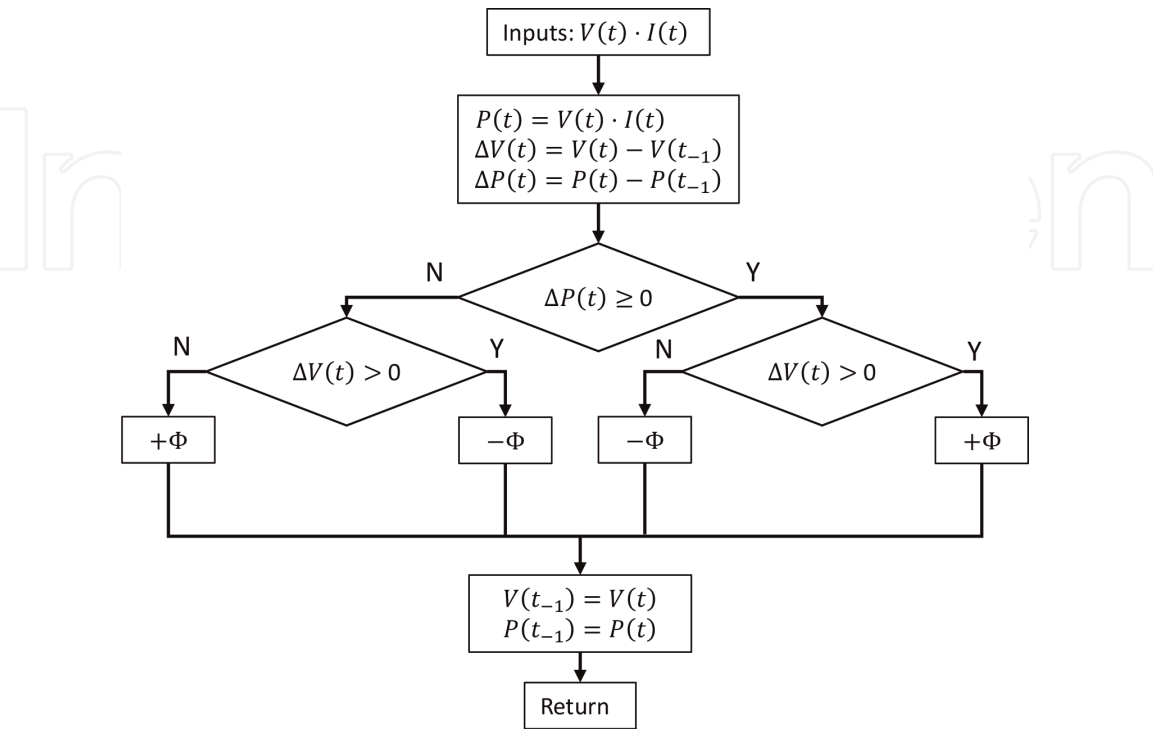

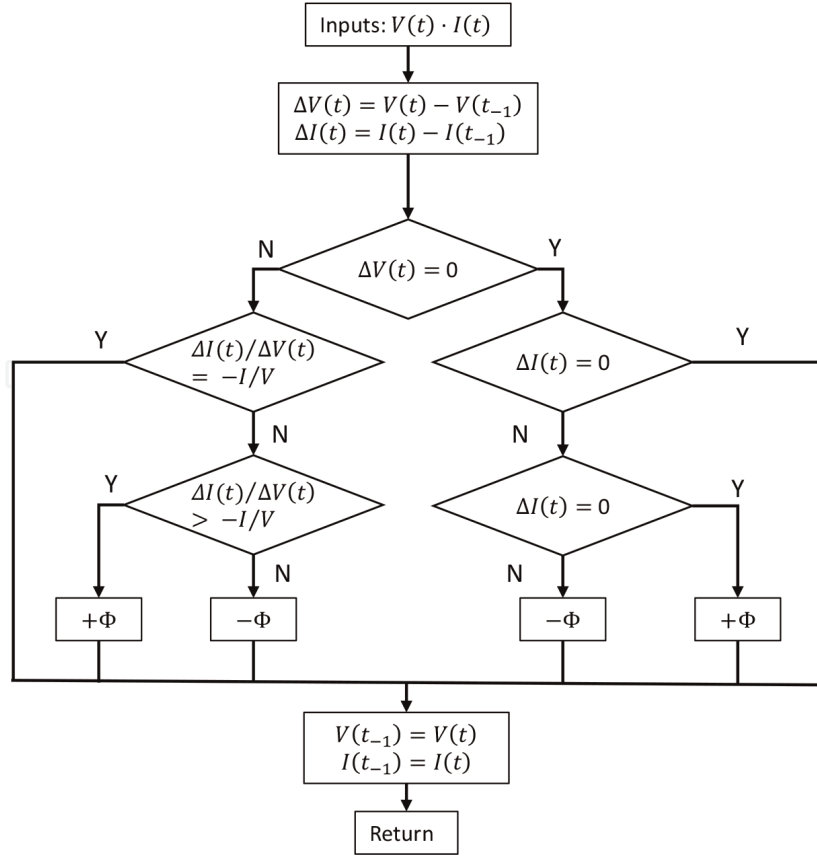**Figure 19.**
P&O algorithm flowchart.

Figure 20.
IC algorithm flowchart.

$$\frac{dP}{dV} = \frac{d(VI)}{dV} = I + V \cdot \frac{dI}{dV} \tag{28}$$

$$\begin{cases} \dfrac{dI}{dV} = -\dfrac{I}{V}, \text{ at } MPP \\[2mm] \dfrac{dI}{dV} > -\dfrac{I}{V}, \text{ left of } MPP \\[2mm] \dfrac{dI}{dV} < -\dfrac{I}{V}, \text{ right of } MPP \end{cases} \tag{29}$$

In practical application the equality condition rarely exists. Moreover, the conductance instantaneous value is related to perturbation size; because of that a marginal error (ε) is introduced. The IC algorithm considers the MPP reached when the operating point is within a certain error margin (Eq. (30)):

$$\left| I + V \cdot \frac{dI}{dV} \right| < \varepsilon \tag{30}$$

Using nested control system, the output perturbation of the MPPT algorithm is used as a reference for the internal control loops that are described in the next subsection.

2.4.2 Current loop

A change of the TEG operating point and a change of converter output current are alike. In order to control the output current, an average current control loop is used. The output of the MPPT algorithm is used as a reference for the current

control loop. The average current of the inductor is related to the output current, and the stationary relation between input and output current is reported in Eq. (31):

$$I_i = \frac{I_o \cdot D_A}{1 - D_B} \tag{31}$$

The system-state variables of a NIBB converter are reported in Eq. (32); the model of the system is expressed in matrixial form in Eq. (33):

$$x = \begin{bmatrix} i_L \\ v_C \end{bmatrix} \tag{32}$$

$$\dot{x} = \begin{bmatrix} 0 & -\overline{D_B}/L \\ \frac{\overline{D_B}}{C} & -1/R \cdot C \end{bmatrix} \cdot x + \begin{bmatrix} D_A/L \\ 0 \end{bmatrix} \cdot V_i \tag{33}$$

The Laplace form of linearized model of the converter is reported in Eq. (34):

$$\begin{cases} i_L(s) = \dfrac{V_{in}}{sL} \cdot d_A(s) + \dfrac{V_o}{sL} \cdot d_B(s) - \dfrac{\overline{D_B}}{sL} \cdot v_o(s) \\ v_o(s) = -\dfrac{I_L}{sC} \cdot d_B(s) + \dfrac{\overline{D_B}}{sC} \cdot i_L(s) - \dfrac{1}{sRC} \cdot v_o(s) \end{cases} \tag{34}$$

The system is characterized by two control inputs (d_A, d_B), but as shown in Section 2.3, it is possible to consider them one at a time if the system is in buck or boost region. In order to have only one control variable also in the buck-boost region, it is possible to fix one leg, i.e., boost leg, and command only the other. Another way is to use the same command: the two duty cycles $(d_A = d_B)$. The buck transfer function between duty cycle and current is reported in Eq. (35), and the boost transfer function between duty cycle and current is reported in Eq. (36). The effect of the output capacitor series resistance is neglected:

$$G_{di} = \frac{R}{(1 + sRC_{out})} \tag{35}$$

$$G_{di} = \frac{V_{in}}{(1 - D_B)} \cdot \frac{sRC + 2}{R(1 - D_B)^2 + sL + s^2RLC_o} \tag{36}$$

The proposed controller for the average current control loop is a simple proportional integrative (PI) controller, the current reference comes from the MPPT algorithm, and the output current is the feedback. **Figure 21** shows the system transfer function and the controller behavior.

2.5 Simulations and design validation

The complete system is simulated in a model-based environment; thermoelectric generator is modeled using the mathematical model described in Section 2.1, while for the DC-DC converter and the load, it is used as a package to use circuital and power components inside the environment; values of **Table 1** are used. Sense blocks are placed before and after the converter, and measures are used in the control block in order to generate the correct commands. The complete system functional blocks are reported in **Figure 22**. For the purpose of validating the single control algorithm, the blocks are tested separately. **Figure 23** shows a detail of the P&O MPPT algorithm simulation: the algorithm's output is the equivalent resistance
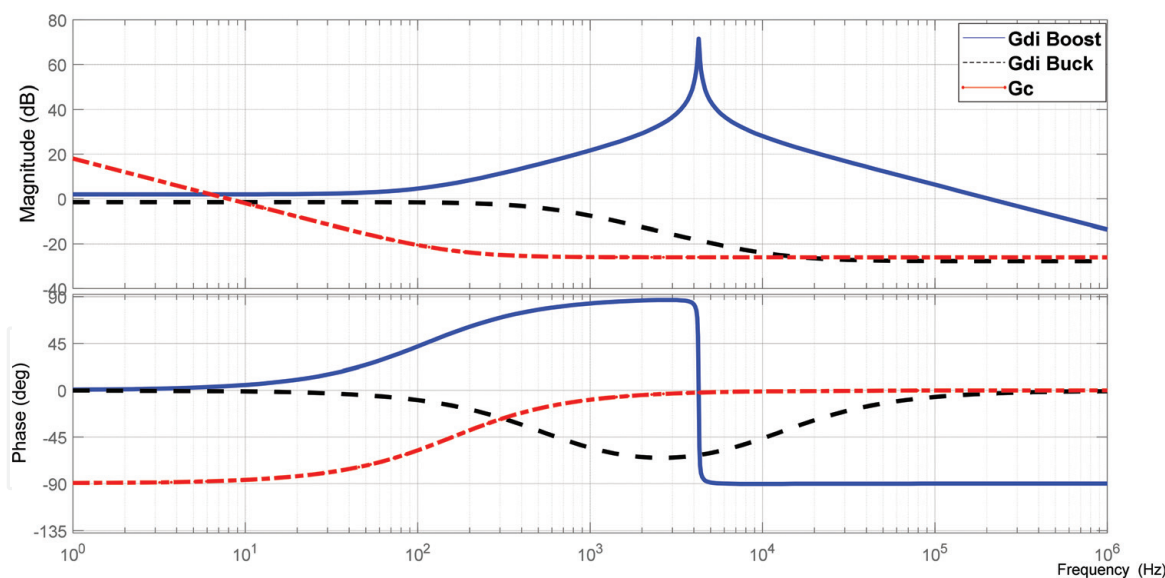
Figure 21.
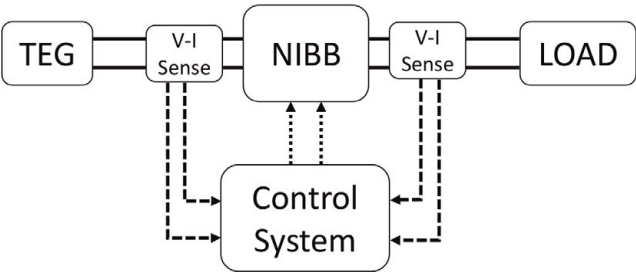*System transfer functions and controller transfer function.*

Figure 22.
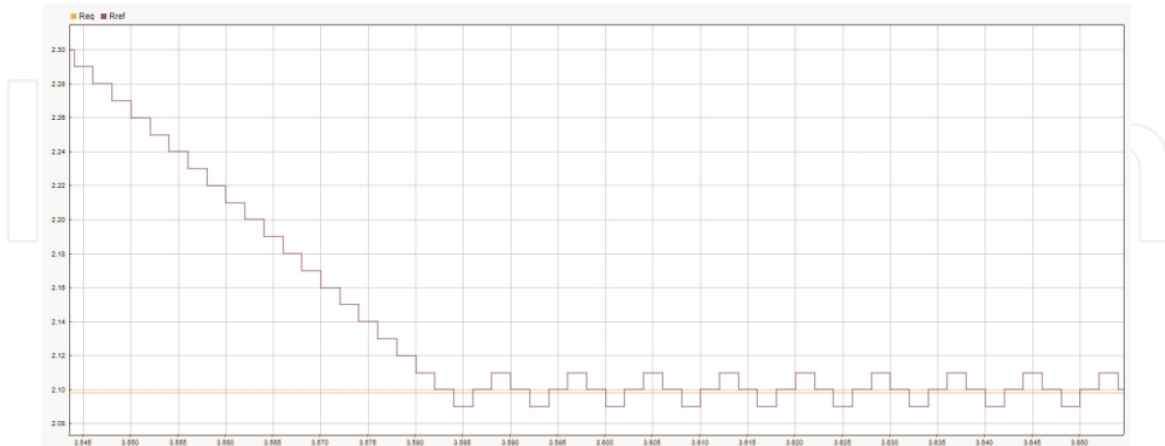*Wasted heat energy recovery system block diagram.*

Figure 23.
Maximum point tracking.

placed after the TEG. The operating point is fixed; the value of the resistance seen by the TEG is initialized at a wrong value, after some iteration; and according to the maximum power transfer theorem, the maximum power point is reached. During the steady-state operation, the resistance value continuously changes its value as seen in Section 2.4.1.
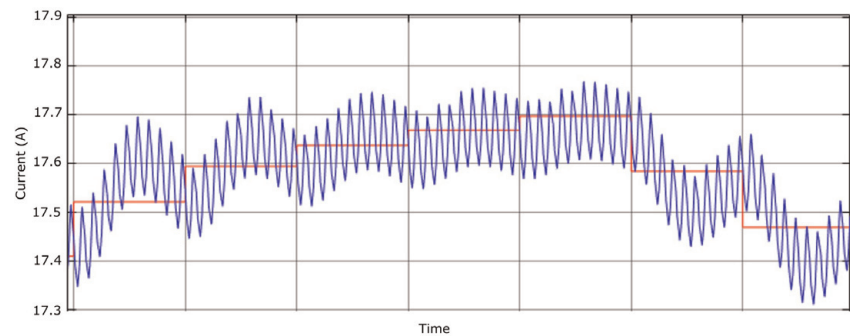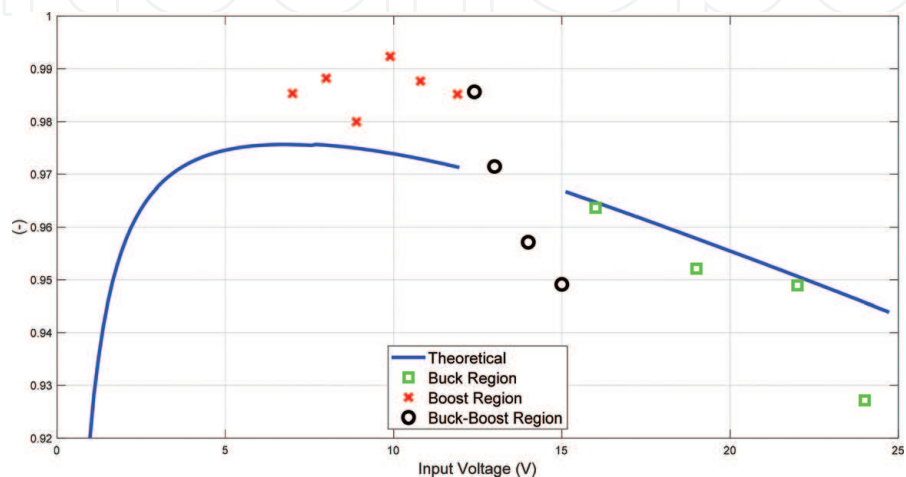
Figure 24.
Average current control.

Figure 25.
Efficiency as a function of input voltage.

Figure 24 shows the average current loop behavior with variable reference. The reference changes with steps like the behavior of the MPPT algorithm output. The reported current is the inductor current. In order to realize a nested control loop, it is important that the inner current loop band is larger than the outer MPPT loop.

A NIBB prototype is realized using the designed components. In order to validate the functionality and loss estimation, some power tests are carried out. **Figure 25** shows the overlapping of the theoretical efficiency and the real efficiency obtained with open-loop commands. The difference from real data and estimation is due to the discrepancy of parasitic values: estimation plot is referred to **Table 1**; real selected components have slowly better parameters.

3. Conclusions

A comprehensive methodology for the design of a wasted heat energy recovery system is given. The general approach is to model separately the single stages starting from physical characteristic and derivate the resulting design constraints. Starting from the characteristic of a thermoelectrical generator cell, the mathematical model and the equivalent electrical model are obtained; after this step it was possible to design the TEG pack. From this point the generator is considered a general input for the power converter. Different topologies are analyzed, and all the fundamental design steps are reported for a non-inverting buck-boost converter: as part of the design, a loss estimation analysis was carried out. The control system is described as nested control loops. Two maximum power point tracking algorithms

are presented illustrating their characteristics and peculiarity. A state-space averaging method is used to obtain the converter transfer function in order to design a proper controller. Finally, simulation results and converter efficiency are shown in the last section. There are many possible advancements in this field from hardware and software point of view: development of new thermoelectric cells; use of more efficient power devices, for example, Gan FETs, in order to increase frequency and reduce passive components; and, also, development of faster and more efficient control algorithm are only some examples.

Acknowledgements

Author details

Dario Gandini[1], Marcello Chiaberge[1]* and Andrea Nepote[2]

1 Department of Electronics and Telecommunications (DET), Politecnico di Torino, Turin, Italy

2 Magneti Marelli, Technology Innovation, Italy

*Address all correspondence to: marcello.chiaberge@polito.it

IntechOpen

References

[1] Yu C, Chau KT. Thermoelectric automotive waste heat energy recovery using maximum power point track. Energy Conversion and Management. 2009;**50**:1506-1512. DOI: 10.1016/j.enconman.2009.02.015

[2] Liu C, Chen P, Li K. A 500 W low-temperature thermoelectric generator: Design and experimental study. International Journal of Hydrogen Energy. 2014;**39**:15497-15505. DOI: 10.1016/j.ijhydene.2014.07.163

[3] Ji D, Romagnoli A. Modelling and design of thermoelectric generator for waste heat recovery. In: ASME Proceedings 9th Symposia: Fluid Mechanics (Fundamental Issues and Perspectives; Industrial and Environmental Applications); Multiphase Flow and Systems (Multiscale Methods; Noninvasive Measurements; Numerical Methods; Heat Transfer; Performance); Transport Phenomena (Clean Energy; Mixing; Manufacturing and Materials Processing); Turbulent Flows; V01BT22A002. 2016. DOI: 10.1115/FEDSM2016-7833

[4] Esram T, Chapman PL. Comparison of photovoltaic array maximum power point tracking techniques. IEEE Transactions on Energy Conversion. June 2007;**22**(2):439-449. DOI: 10.1109/TEC.2006.874230

[5] Nagayoshi H, Kajikawa T, Sugiyama T. Comparison of maximum power point control methods for thermoelectric power generator. In: Twenty-First International Conference on Thermoelectrics (ICT '02). 2002. DOI: 10.1109/ICT.2002.1190358

[6] Laird I, Lovatt H, Savvides N, Lu D, Agelidis VG. Comparative study of maximum power point tracking algorithms for thermoelectric generators. In: 2008 Australasian Universities Power Engineering Conference. 2008. DOI: 10.1109/ICT.2002.1190358

[7] Twaha S, Zhu J, Yan Y, Li B, Huang K. Performance analysis of thermoelectric generator using dc-dc converter with incremental conductance based maximum power point tracking. Energy for Sustainable Development. 2017;**37**:86-98. DOI: 10.1016/j.esd.2017.01.003

[8] Montecucco A, Siviter J, Knox AR. Simple, fast and accurate maximum power point tracking converter for thermoelectric generators. In: 2012 IEEE Energy Conversion Congress and Exposition (ECCE). 2012. DOI: 10.1109/ECCE.2012.6342530

[9] Lee JH, Bae H, Cho BH. Advanced incremental conductance MPPT algorithm with a variable step size. In: 2006 12th International Power Electronics and Motion Control Conference. 2006. DOI: 10.1109/EPEPEMC.2006.4778466

[10] Liu B, Duan S, Liu F, Xu P. Analysis and improvement of maximum power point tracking algorithm based on incremental conductance method for photovoltaic array. In: 2007 7th International Conference on Power Electronics and Drive Systems. 2007. DOI: 10.1109/PEDS.2007.4487768